PHYSICAL REVIEW A VOLUME 5, NUMBER 1 JANUARY 1972

Photoionization of the Noble Gases: Cross Sections and Angular Distributions

David J. Kennedy*
School of Physics, Georgia Institute of Technology, Atlanta, Georgia 30332

and

Steven Trent Manson
Department of Physics, Georgia State University, Atlanta, Georgia 30303

(Recieved 12 July 1971)

Photoionization calculations in the noble gases Ne(L shell), Ar(L and M shell), Kr(M and N shell), and Xe(M, N, and O shell) using Hartree-Fock (HF) wave functions for the outgoing photoelectron are reported. Total cross sections are presented and compared with experiment. Subshell cross sections are also given and unusual features are pointed out in an effort to stimulate direct measurements of subshell cross sections via the technique of photoelectron spectroscopy. The relation between our work and the *intra*channel coupling of the Fano continuum configuration-interaction theory is discussed. The asymmetry parameter β of the angular distribution of the photoelectrons, $1+\beta P_2(\cos\theta)$, is calculated in HF-length, HF-velocity, and Hartree-Slater (HS) approximations. The results show remarkable agreement among the β's resulting from the several approximations despite the rather different cross sections they predict. Good agreement with recent experimental results is found and the need for further experimental work is pointed out. Extremely oscillatory behavior of the energy dependence of β is found and the reasons for such behavior are discussed.

I. INTRODUCTION

The ionization of an atom by incoming photons, the process of photoionization, is of importance in plasma physics, atmospheric, space, and astrophysics, as well as in the area of radiation physics. At energies below about 10 keV the cross section for photoionization is equal to the photoabsorption cross section since other processes which lead to attenuation of photons, such as Compton scattering and brehmstrahlung, are negligible.[1] Until recently, essentially all of the measurements were of the absorption of photons,[2] but advances in experimental techniques over the last few years[3] have begun to stimulate direct measurements of the distribution of photoelectrons in energy and angle.[4-14] Thus, data are being obtained on the photoionization of individual atomic subshells in addition to the previous total-cross-section results. Most of these recent and forthcoming experiments, as well as much of the previous data, concern the noble gases, which, being monatomic gases at room temperature, are relatively simple to work with in the laboratory. It is therefore of interest to have theoretical estimates of the total, subshell, and angular cross sections in the noble gases.

In this paper we present results of calculations on neon, argon, krypton, and xenon. These calculations have been performed with a threefold purpose in mind. The first is to provide a background for the interpretation of experimental results. The second is to provide detailed, reasonably accurate data on subshell cross sections and photoelectron angular distributions to aid experimenters in choosing which subshells and energies to investigate. The third is to obtain results using essentially the best possible single-particle wave functions (Hartree-Fock functions with complete exchange) for all of the noble gases, to discover where such a calculation is adequate and where further refinements in the theory, such as interchannel coupling,[15,16] are important. Thus, these calculations are to be considered a first approximation to a description of the photoionization process. They are carried out in such a way as to make them amenable to successive improvements using the Fano continuum configuration-interaction theory.[15,16] The details of the wave functions employed, along with some discussion of the theory of total and subshell cross sections and photoelectron angular distributions, are presented in Sec. II. We have performed calculations on Ne $2s$ and $2p$ subshells; Ar $2s$, $2p$, $3s$, and $3p$; Kr $3s$, $3p$, $3d$, $4s$, and $4p$; and Xe $3s$, $3p$, $3d$, $4s$, $4p$, $4d$, $5s$, and $5p$ subshells. The total and subshell cross sections are presented and compared with experiment and other calculations in Sec. III. Phase shifts and angular distributions are given in Sec. IV. Section V gives a discussion of all results and concluding remarks.

Recently a study somewhat similar in scope to ours has been carried out by Amusia, Cherepkov, and Chernysheva[17] who considered multielectron correlations in the final state using the random-phase approximation,[18] starting with essentially Hartree-Fock wave functions. This work complements ours since it is concerned primarily with

total photoabsorption cross sections, while we are mainly interested in subshell cross sections and angular distributions. In another sense, however, the work of Ref. 17 is an advance over the results we report since it deals with multiparticle effects.

II. THEORY

If the wave function of an atom is represented in the form of an antisymmetric product of single-particle wave functions, the cross section for photoionization of an electron in the nlth subshell is given in the dipole approximation by

$$\sigma_{nl}(\epsilon)=\tfrac{4}{3}\pi^2\alpha a_0^2[N_{nl}(\epsilon-\epsilon_{nl})/(2l+1)] \times[lR^2_{\epsilon,l-1}+(l+1)R^2_{\epsilon,l+1}]. \quad (1)$$

Here ϵ_{nl} (in rydbergs) is the binding energy of an electron in the nlth subshell, α is the fine-structure constant ($\sim\frac{1}{137}$), a_0 is the Bohr radius (5.29×10^{-9} cm), N_{nl} is the number of electrons in the subshell, and ϵ (in rydbergs) is the energy of the ionized electron, i.e., $h\nu=\epsilon-\epsilon_{nl}$, where $h\nu$ is the energy of the incident photon. The radial dipole matrix elements are

$$R_{\epsilon,l\pm1}=\int_0^\infty P_{nl}(r)\,r\,P_{\epsilon,l\pm1}(r)\,dr\,, \quad (2)$$

where $P_{nl}(r)/r$ and $P_{\epsilon,l\pm1}(r)/r$ are the radial parts of the single-particle wave functions of the initial (discrete) and final (continuum) states, respectively, satisfying the normalization conditions

$$\int_0^\infty P_{nl}(r)^2\,dr=1\,, \quad (3)$$

$$P_{\epsilon l}(r)\underset{r\to\infty}{\rightarrow}\pi^{-1/2}\epsilon^{-1/4}\sin[\epsilon^{1/2}r-\tfrac{1}{2}l\pi-\epsilon^{-1/2}\ln2\epsilon^{1/2}r+\sigma_l(\epsilon)+\delta_l(\epsilon)]\,, \quad (4)$$

with $\sigma_l(\epsilon)=\arg\Gamma(l+1-i\epsilon^{-1/2})$, and $\delta_l(\epsilon)$ is the phase shift. This normalization of $P_{\epsilon l}(r)$ is the usual normalization of continuum wave functions per unit energy range.

The matrix element given by Eq. (2) is known as the dipole length matrix element. If exact wave functions are used, this will be the same as the dipole velocity form of the matrix element given by[19]

$$R_{\epsilon,l\pm1}=\frac{2}{\epsilon-\epsilon_{nl}}\int_0^\infty P_{nl}(r)\times\left(\pm\frac{d}{dr}+\frac{2l+1\pm1}{2r}\right)P_{\epsilon,l\pm1}(r)\,dr\,. \quad (5)$$

In our calculation we consider both forms of the dipole matrix element since their difference provides us with an estimate of the accuracy of our results. There is some indication, however, that the length results are more reliable.[20]

The angular distribution of the photoelectrons ionized by polarized light incident on the nlth subshell is given by[21,22]

$$\frac{d\sigma_{nl}(\epsilon)}{d\Omega}=\frac{\sigma_{nl}(\epsilon)}{4\pi}\,[1+\beta(\epsilon)\,P_2(\cos\varphi)]\,, \quad (6)$$

where φ is the angle between the polarization direction and photoelectron direction, and $P_2(x)=\frac{1}{2}(3x^2-1)$. Unpolarized light can be considered as the incoherent superposition of two polarized beams with one polarization direction lying in the plane defined by the incident photon beam and photoelectron directions, and the other perpendicular to it. For unpolarized light the angular distribution of photoelectrons from the nlth subshell will then be[23]

$$\frac{d\sigma_{nl}(\epsilon)}{d\Omega}=\frac{\sigma_{nl}(\epsilon)}{4\pi}\,[1-\tfrac{1}{2}\beta(\epsilon)\,P_2(\cos\theta)]=A+B\sin^2\theta\,, \quad (7)$$

where θ is the angle between the incident photon beam and the photoelectron direction. Equations (6) and (7) can be obtained from quite general considerations, depending only on the absorption of radiation occurring via an electric dipole process.[24] Deviation from the form of these equations implies the presence of absorption via processes other than electric dipole.[24] The "asymmetry parameter" $\beta(\epsilon)$, however, does depend upon the details of the calculation. Specifically, for LS-coupled antisymmetrized products of single-particle functions the asymmetry parameter is given by[21,22]

$$\beta(\epsilon)=\frac{l(l-1)R^2_{\epsilon,l-1}+(l+1)(l+2)R^2_{\epsilon,l+1}-6l(l+1)R_{\epsilon,l+1}R_{\epsilon,l-1}\cos(\xi_{l+1}(\epsilon)-\xi_{l-1}(\epsilon))}{(2l+1)[lR^2_{\epsilon,l-1}+(l+1)R^2_{\epsilon,l+1}]}\,, \quad (8)$$

with

$$\xi_{l\pm1}(\epsilon)\equiv\delta_{l\pm1}(\epsilon)+\sigma_{l\pm1}(\epsilon)\,. \quad (9)$$

The radial part of the wave function of the continuum electron, $P_{\epsilon l}(r)$, ionized from the nlth subshell is obtained by solving the Hartree-Fock (HF) equation in the frozen core of the positive ion with an nl' hole. We consider only the ^1P multiplet since this is the only one optically accessible from the ^1S ground state of a noble-gas atom. This equation can be written generally for the noble gases

$$\left(\frac{d^2}{dr^2}-\frac{l(l+1)}{r^2}+\epsilon+V(r)\right)P_{\epsilon l}(r)+U(r)=0\,, \quad (10)$$

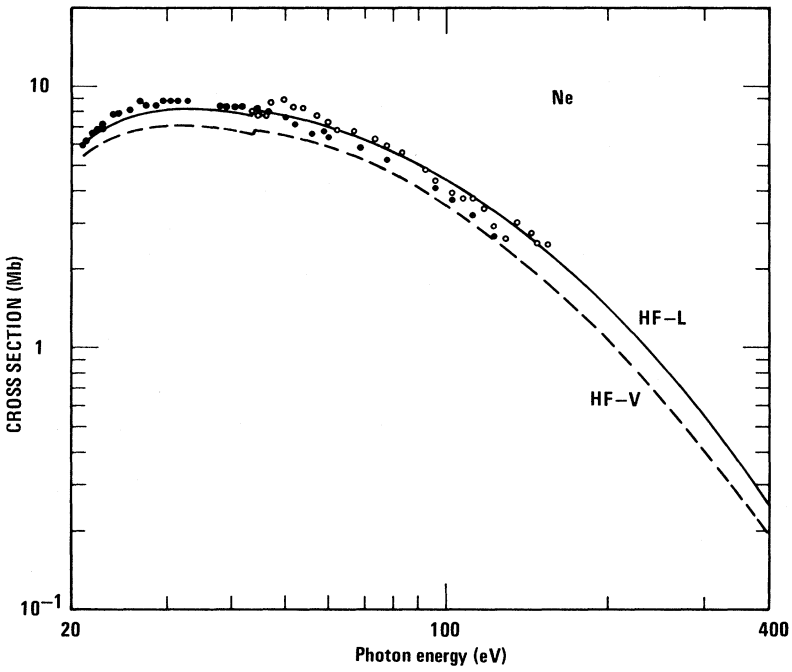

FIG. 1. Total absorption cross section for Ne; data points: closed circles, Ref. 2; open circles, Ref. 44.

where

$$V(r)=(2/r)\{Z-2\sum_n Y^0(ns,ns)-6\sum_n Y^0(np,np)-10\sum_n Y^0(nd,nd)+Y^0(nl',nl')+\tfrac{1}{5}Y^2(nl',nl')\delta_{l+l',3}+[\tfrac{8}{35}Y^2(nl',nl')+\tfrac{22}{231}Y^4(nl',nl')]\delta_{l+l',5}\}\,, \quad (11)$$

$$U(r)=(2/r)X(r)+\sum_n \lambda_{nl}P_{nl}(r)\,, \quad (12)$$

with

$$Y^k(ml,ml)=\frac{1}{r^{k+1}}\int_0^r r'^k P_{ml}(r')^2\,dr' + r^k\int_r^\infty \frac{P_{ml}(r')^2}{r'^{k+1}}\,dr' \quad ; \quad (13)$$

Z is the nuclear charge, and λ_{nl} is the off-diagonal parameters to ensure the orthogonality of $P_{\epsilon l}$ to the P_{nl} of the final-state ion core. The term $(2/r)X(r)$ in Eq. (12) is the exchange interaction between the photoelectron and the ion core. The detailed form of $X(r)$ for the various photoionization processes which we consider is given in the Appendix.

For the discrete orbitals in the wave function for the residual ion, as well as for the initial state, we have several possible choices. A reasonable choice is HF functions for the neutral atom and the ion, so as to include the effects of core relaxation. Such a scheme, however, yields initial and final states in different basis sets which renders it unacceptable for further theoretical improvements owing to the complexity involved. Further, the wave functions for the ion cores of Kr and Xe with inner-shell holes are not readily available. Thus, for our purposes, we use the same discrete orbitals in both the initial and final state. In particular, we employ Hartree-Slater (HS) functions as tabulated by Herman and Skillman[25] since they are central-field functions and further members of the basis set can be easily generated. We use the HS rather than, say, the HF orbitals appropriate to the neutral atom because although the HF wave functions probably approximate the initial state more closely, they are most likely inferior for the ion core so that there does not seem to be any obvious advantage in using HF orbitals of this type.

Performing a Hartree-Fock calculation for the continuum orbital is then equivalent to diagonalizing the intrachannel coupling matrix in the Fano formalism[15] starting with a basis of HS discrete and continuum orbitals so that, in a sense, this calculation represents a first step in the systematic improvement of the simple HS results. Further refinements such as interchannel coupling and configuration interaction in the initial discrete state could then be made using the results of this paper as a starting point.

III. CROSS SECTIONS

A. Total Cross Sections

The computed values of the total cross sections are shown for Ne, Ar, Kr, and Xe in Figs. 1–4, where they are compared with available experimental data.[2] Although the use of double logarithmic scales tends to deemphasize the disagreement

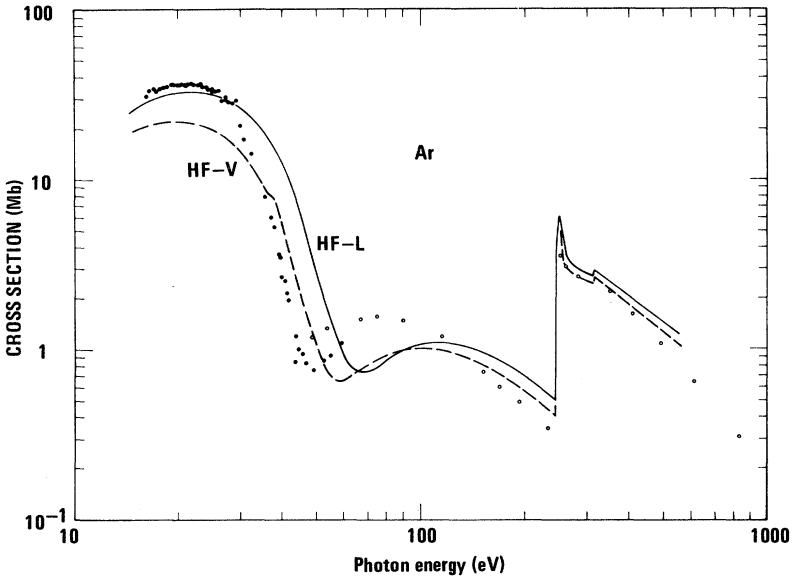

FIG. 2. Total absorption cross section for Ar; data points: closed circles, Ref. 2; open circles, Ref. 44.

between the present theoretical and the experimental results, it does show that the gross structure of the experimental photoionization cross section is reproduced quantitatively by theory over a very wide range of photon wavelengths.

In Ne, there is good agreement, about 10%, at most energies between the theoretical and experimental values of the cross sections. Autoionization processes have been ignored in the present calculations, but there is nevertheless very good agreement between the values of the cross section found using the length formulation and the data of Samson[2] in the near-threshold region. The difference between length and velocity results for Ne remains quite constant at all energies, being about 15%. At the L_1 edge, the theory predicts a jump of about 5%, but this does not appear in Samson's data. The data of Ederer and Tomboulian,[26] however, are in good agreement with the length results in this energy region and do show a jump at the L_1 threshold. From the L edge down to about 100 Å, Samson's data lie between the present length and velocity results, and tend towards the velocity values at the shorter wavelengths.

Agreement between the experimental and length-formulation values is also good for the first few

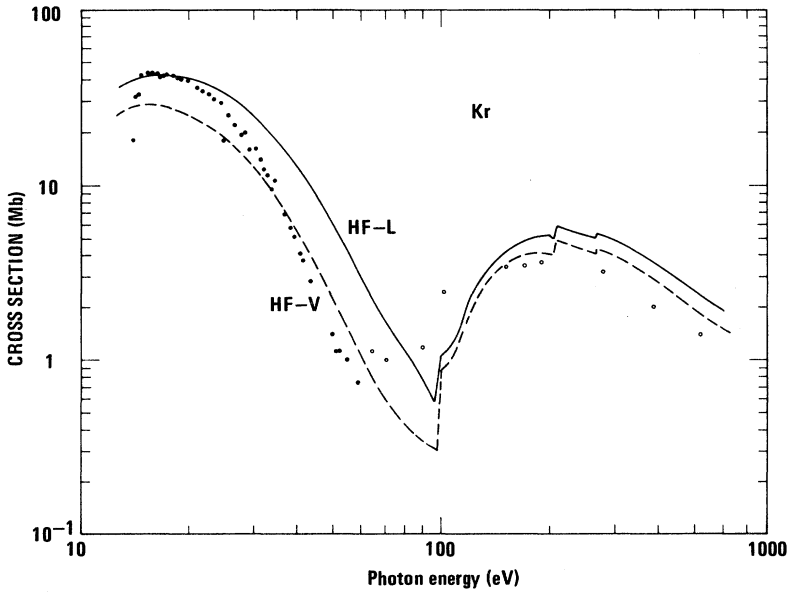

FIG. 3. Total absorption cross section for Kr; data points: closed circles, Ref. 2; open circles, Ref. 44.

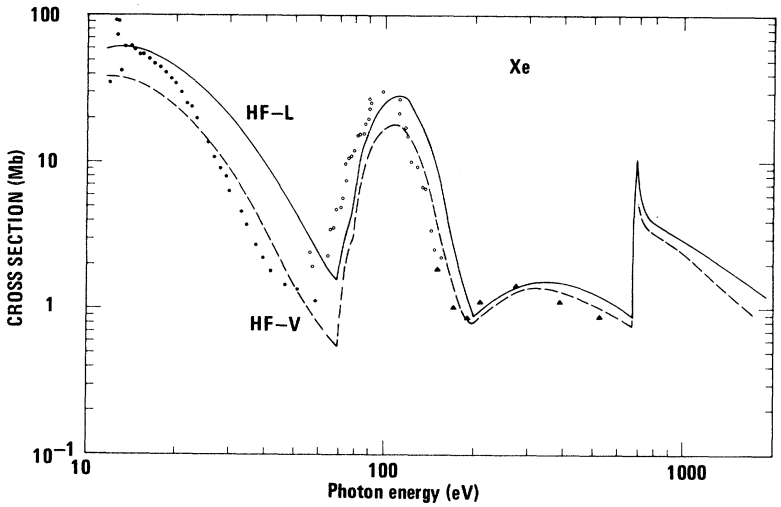

FIG. 4. Total absorption cross section for Xe; data points: closed circles, Ref. 2; open circles, Ref. 26; triangles, Ref. 44.

electron volts above threshold for Ar, Kr, and Xe. All three sets of theoretical HF curves show an initial rise in the cross section of the same magnitude as is found experimentally. However for these atoms the difference between the length and velocity results for the outer-shell contribution is much greater than in Ne, being about 50%. The experimental data appear to fall off more rapidly than either length or velocity curves and reach a minimum value some 10–20 eV before the theoretical curves. It is not clear whether this is due to the s-subshell cross section being too small, or to the theoretical Cooper minimum occurring at too large an energy, or some combination of these effects. In Xe, where there is a second Cooper minimum due to the $4d$ subshell, there is good agreement in the energy range between the two Cooper minima.

At photon energies higher than the Cooper minima, when the inner-shell contributions begin to dominate the total cross section, the agreement between length and velocity values improves, and in general there is closer agreement between theory and experiment.

Apart from those spectral regions where one particular subshell contributes predominantly to the total cross section, little can be inferred directly at present from experiment as to the validity of the subshell calculations. In fact a major aim of this work is to stimulate experimental measurements of subshell cross sections via the technique of photoelectron spectroscopy. One must resort therefore to a comparison of the various theoretical results to obtain some guide to the over-all accuracy of the present calculations. This will be considered in Sec. III B 5.

B. Subshell Cross Sections

The total subshell photoionization cross sections ($l \rightarrow l+1$ plus $l \rightarrow l-1$ channels) resulting from our HF calculations are given for the $2s$ and $2p$ in Ne in Table I; Ar $2s$, $2p$, $3s$, and $3p$ in Table II; Kr $3s$, $3p$, $3d$, $4s$, and $4p$ in Table III; and Xe $3s$, $3p$, $3d$, $4s$, $4p$, $4d$, $5s$, and $5p$ in Table IV. We present the results in both the length and velocity formulations to provide an estimate of the uncertainty. In Secs. III B 1–III B 4, these data are discussed in detail

1. *Outer Subshells*

The results of our calculations for the Ne $2p \rightarrow \epsilon d$ transition are presented in Fig. 5 along with the HS results. The HF-length (HF-L) and the HF-velocity (HF-V) cross sections agree reasonably well with each other, with the HF-L always larger than HF-V. The HS data are also in fairly good agreement, being closer to HF-L near threshold

TABLE I. Hartree-Fock results for the photoionization cross sections, in Mb, for individual subshells in Ne, as a function of the photoelectron energy ϵ, in Ry. HF-L and HF-V refer to calculations in the length and velocity formulations.

	$2p$		$2s$	
ϵ (Ry)	HF-L	HF-V	HF-L	HF-V
0	5.44	4.96	2.84−1	2.53−1
0.5	7.80	6.89	4.40−1	3.68−1
1.0	8.23	7.12	5.24−1	4.82−1
1.5	7.98	6.78	5.70−1	5.27−1
2.0	7.50	6.30	5.89−1	5.46−1
3.0	6.44	5.28	5.81−1	5.39−1
4.0	5.43	4.35	5.43−1	5.04−1
6.0	3.76	2.91	4.52−1	4.17−1
8.0	2.63	1.97	3.70−1	3.39−1
10.0	1.89	1.37	3.04−1	2.78−1
15.0	8.72−1	6.04−1	2.00−1	1.78−1
20.0	4.28−1	2.93−1	1.37−1	1.20−1
30.0	1.33−1	9.43−2	7.10−2	6.13−2

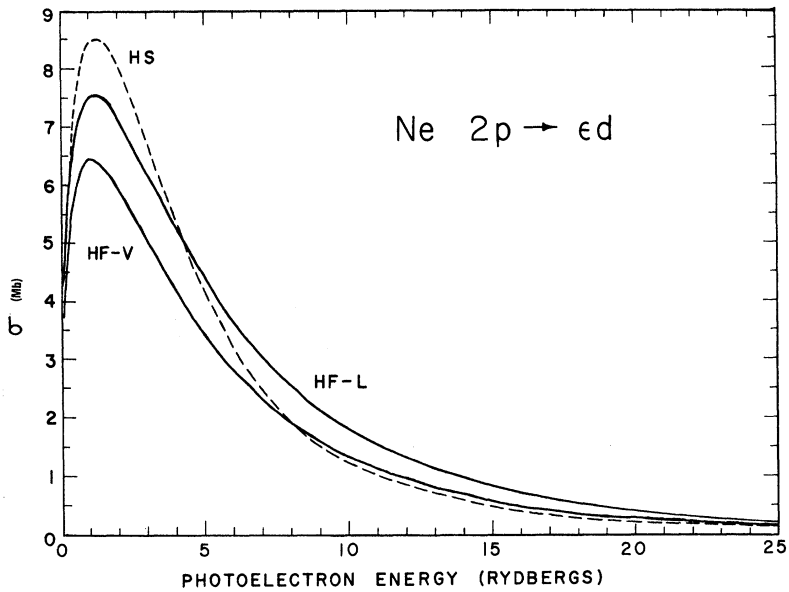

FIG. 5. Ne $2p \rightarrow \epsilon d$ partial photoionization cross section.

and nearer HF-V in the higher-energy region.

The situation is substantially different for the outer-shell $np \rightarrow \epsilon d$ transitions in Ar, Kr, and Xe which are shown in Figs. 6–8. The most striking feature of all three of these figures is their great similarity to each other as well as their differences from the Ne results. This is due to the fact that although these are all outermost p subshells, Ar, Kr, and Xe have a Z value just below the value required to bind a new d orbital in the atom's ground state. Thus the character of the ϵd continuum orbitals is similar for Ar, Kr, and Xe but rather different for Ne.

A maximum occurs near threshold in each case with HF-L more than 50% larger than HF-V in Ar, increasing through Kr to almost 70% in Xe. The HS results show a much higher and narrower peak somewhat closer to threshold. A Cooper minimum appears in all of these cases with the minimum occurring at highest energy in HF-L and lowest in HS. In the energy region just above the Cooper minimum, the HF-V cross section is greater than HF-L, and the over-all agreement between the different approximations is much better at the higher energies than at the lower. At higher energies the HS results are close to the HF-V while near-threshold agreement with HF-L is better in all three atoms, similar to the trends found in Ne and in the experimental data.

The $4d \rightarrow \epsilon f$ photoionization cross section in Xe, shown in Fig. 9, is the only other transition we have considered that has a Cooper minimum. Here

TABLE II. Hartree-Fock results for the photoionization cross sections, in Mb, for individual subshells in Ar, as a function of the photoelectron energy ϵ, in Ry. HF-L and HF-V refer to calculations in the length and velocity formulations.

	3p		3s		2p		2s	
ε (Ry)	HF-L	HF-V	HF-L	HF-V	HF-L	HF-V	HF-L	HF-V
0.0	2.46+1	1.85+1	7.20−2	3.98−2	7.57	7.27	3.18−1	3.23−1
0.5	2.57+1	1.91+1	2.26−1	1.48−1	4.03	3.85	3.35−1	3.42−1
1.0	2.98+1	1.73+1	2.95−1	2.28−1	2.94	2.79	3.33−1	3.37−1
1.5	1.97+1	9.74	3.42−1	2.72−1	2.67	2.52	3.24−1	3.28−1
2.0	9.13	3.69	3.61−1	2.92−1	2.59	2.43	3.14−1	3.17−1
3.0	1.12	4.08−1	3.59−1	2.95−1	2.53	2.36	2.91−1	2.93−1
4.0	3.64−1	5.08−1	3.37−1	2.76−1	2.43	2.25	2.72−1	2.72−1
6.0	7.22−1	7.77−1	2.79−1	2.28−1	2.14	1.97	2.45−1	2.44−1
8.0	8.34−1	7.29−1	2.30−1	1.85−1	1.92	1.74	2.27−1	2.24−1
10.0	7.66−1	6.08−1	1.90−1	1.50−1	1.70	1.54	2.11−1	2.08−1
15.0	4.73−1	3.51−1	1.18−1	9.17−2	1.26	1.12	1.75−1	1.72−1
20.0	2.89−1	2.23−1	7.94−2	6.17−2	9.86−1	8.66−1	1.47−1	1.44−1
30.0	1.36−1	1.11−1	4.21−2	3.36−2	6.42−1	5.51−1	1.08−1	1.04−1

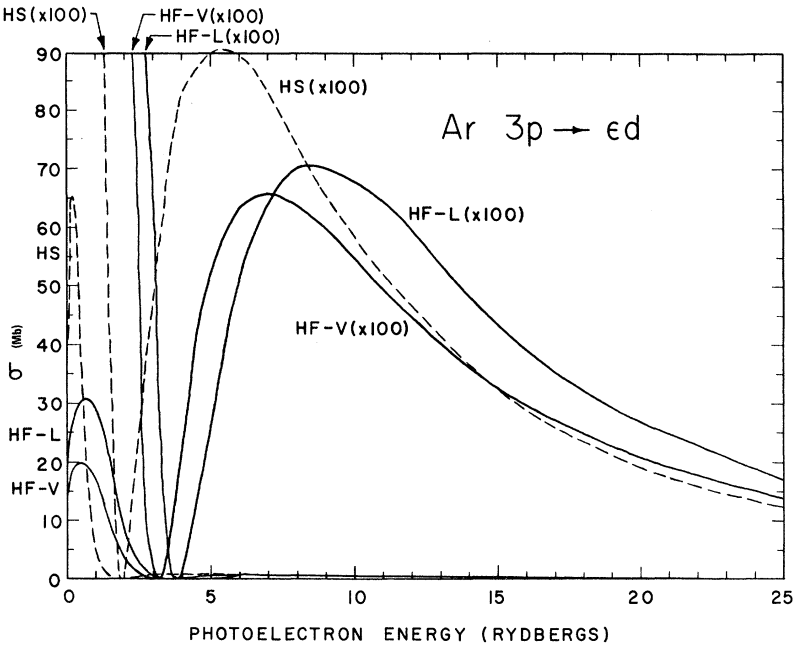

FIG. 6. Ar $3p \rightarrow \epsilon d$ partial photoionization cross section.

again HF-L is more than 50% greater than HF-V near threshold and the HS peak is much too high, by almost an order of magnitude, and too low in energy; the Cooper minimum occurs at the highest energy for HF-L and lowest for HS, and HF-L is greater than HF-V except just above the minimum. Again the HS curve is closest to HF-V at the higher energies and to HF-L near threshold.

The results for the outermost s subshells are shown in Tables I–IV for Ne $2s$, Ar $3s$, Kr $4s$, and Xe $5s$, respectively. These cross sections all have the same general shape. The HF-L results always lie above the HF-V, by less than 10% in Ne up to a maximum of over 35% in Xe. The cross section predicted by the HS approximation (not shown) agrees well for Ne, but is too high in the neighborhood of the maximum by 20–30% for the others. In all four of these cases it approaches the HF-V result at higher energies.

An interesting feature of the HF cross sections for the outer s subshells in Kr and Xe is the occurrence of a Cooper minimum just above threshold which is shown in Fig. 10. Here it is seen that the minimum is more pronounced for HF-V than HF-L, and does not even appear above threshold in the HS results. This minimum, a zero minimum since only one channel contributes for s states, is so small as to be masked in the total cross section,

TABLE III. Hartree-Fock results for the photoionization cross sections, in Mb, for individual subshells in Kr, as a function of the photoelectron energy ϵ, in Ry. HF-L and HF-V refer to calculations in the length and velocity formulations.

	$4p$		$4s$		$3d$		$3p$		$3s$	
ϵ (Ry)	HF-L	HF-V	HF-L	HF-V	HF-L	HF-V	HF-L	HF-V	HF-L	HF-V
0	3.66+1	2.60+1	1.09−4	6.68−3	5.44−1	5.40−1	8.47−1	8.33−1	1.99−1	1.92−1
0.5	3.36	2.14+1	3.80−2	1.70−2	7.41−1	7.06−1	7.15−1	6.97−1	2.08−1	2.00−1
1.0	3.08+1	1.69+1	1.08−1	7.01−2	9.36−1	8.74−1	5.82−1	5.63−1	2.07−1	1.99−1
1.5	2.01+1	9.87	1.52−1	1.07−1	1.49	1.35	5.74−1	5.52−1	2.03−1	1.94−1
2.0	1.23+1	5.36	1.77−1	1.30−1	2.12	1.87	5.83−1	5.57−1	1.98−1	1.88−1
3.0	4.36	1.55	1.95−1	1.50−1	3.15	2.70	6.12−1	5.81−1	1.89−1	1.79−1
4.0	1.65	5.17−1	1.95−1	1.50−1	3.90	3.29	6.35−1	5.99−1	1.82−1	1.72−1
6.0	3.62−1	1.77−1	1.74−1	1.33−1	4.70	3.85	6.58−1	6.16−1	1.74−1	1.62−1
8.0	1.77−1	1.42−1	1.47−1	1.10−1	4.82	3.87	6.67−1	6.20−1	1.65−1	1.53−1
10.0	1.50−1	1.37−1	1.22−1	8.97−2	4.69	3.72	6.59−1	6.10−1	1.55−1	1.43−1
15.0	1.26−1	1.16−1	7.81−2	5.71−2	3.87	2.99	6.03−1	5.52−1	1.32−1	1.21−1
20.0	9.68−2	9.31−2	5.37−2	4.02−2	3.00	2.27	5.32−1	4.85−1	1.13−1	1.03−1
30.0	6.57−2	6.16−2	3.19−2	2.37−2	1.74	1.28	4.05−1	3.67−1	8.66−2	7.83−2

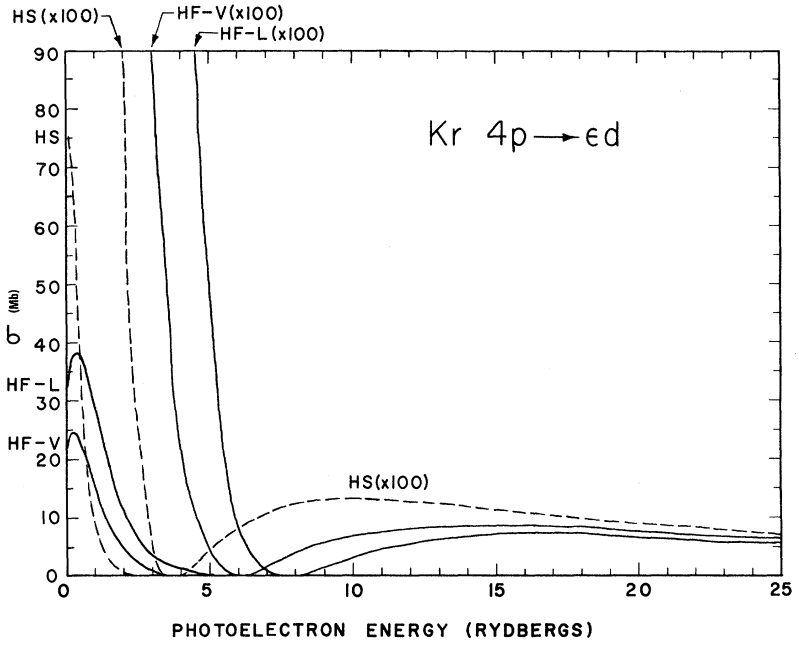

FIG. 7. Kr $4p \rightarrow \epsilon d$ partial photoionization cross section.

but might be seen if the individual subshells were investigated via the technique of photoelectron spectroscopy.

2. *Inner Subshells*

The photoionization cross section for the $3p \rightarrow \epsilon d$ transition in Kr is shown in Fig. 11. An unusual feature here is the nonzero minimum which occurs in all three approximations between 1 and 2 Ry above threshold. This minimum is much more pronounced in HF-L and HF-V than in the HS approximation,[27] and it is not obscured by the addition of the $3p \rightarrow \epsilon s$ channel as shown in Table III. Thus, while the minimum does not show up in the total photoabsorption cross section, it should appear in the photoelectron spectrum from the $3p$ subshell and seems to be an excellent case for experimental study.

This minimum is produced by the variation of the overlap, as a function of energy, of the ϵd with the $3p$ wave function. This is the same as the cause of the Cooper minimum except that in this case the

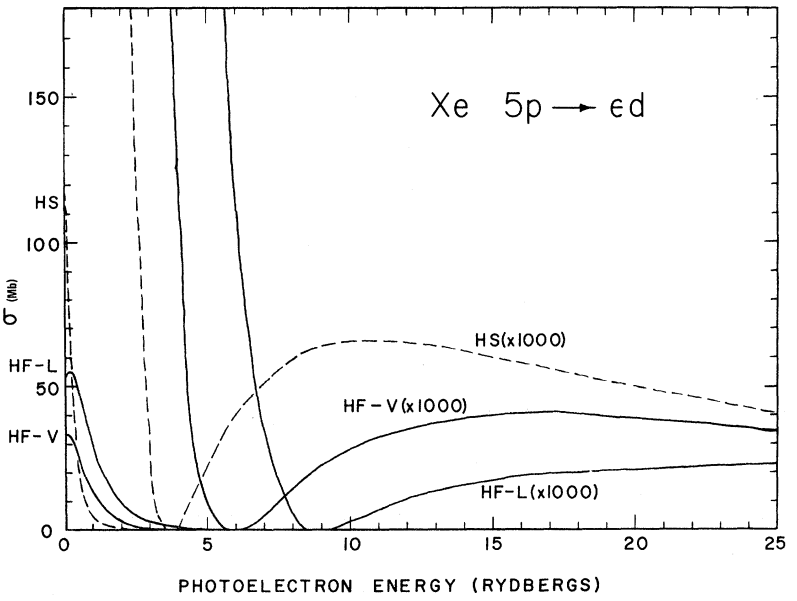

FIG. 8. Xe $5p \rightarrow \epsilon d$ partial photoionization cross section.

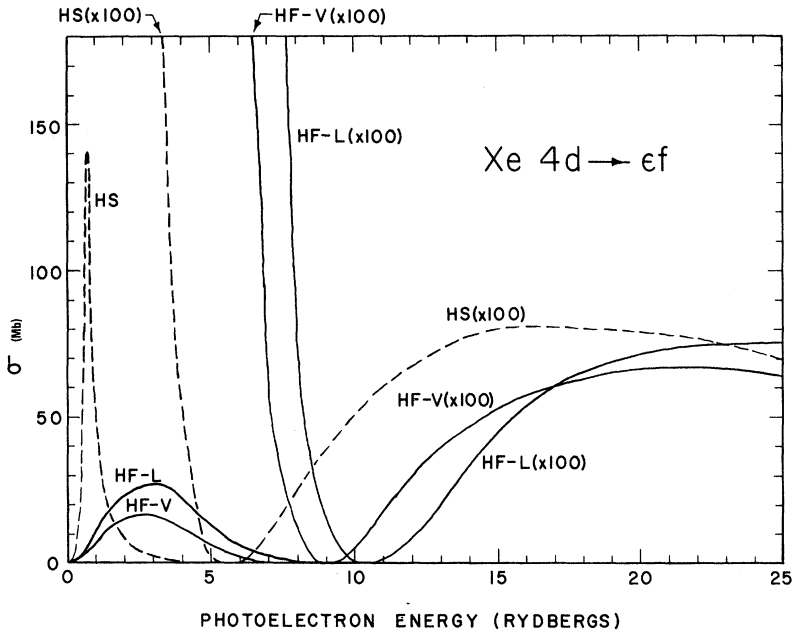

FIG. 9. Xe $4d \rightarrow \epsilon f$ partial photoionization cross section.

local minimum is not a zero minimum because the variation of overlap occurs primarily in the outer part of the discrete wave function. The major part of the matrix element comes from the intermediate and inner part of the discrete function where the continuum solution does not change much with energy; the major portion of the matrix element is thus relatively constant.

A similar effect occurs in the Xe $4p \rightarrow \epsilon d$ transition, but it is much less pronounced and obscured by the addition of the $4p \rightarrow \epsilon s$ channel as is shown in Table IV.

Figure 12 shows results for the photoionization of xenon in the vicinity of the $3d$ ($M_{4,5}$) thresholds together with the experimental results of Deslattes.[28] The agreement between HF-L, HF-V, and experiment is quite good, while the HS curve is quite far off, giving only the correct qualitative behavior. Here an adjustment was made in the calculated cross sections for purposes of comparison with experiment: The spin-orbit splitting of the $M_{4,5}$ subshell into $3d_{3/2}$ and $3d_{5/2}$ (M_4 and M_5) components has been introduced by weighting the cross section for this subshell by 0.4 and 0.6, respectively, and uniformly translating the individual contributions to the experimental thresholds. This adjustment is made to show how realistic nonrelativistic calculations can be used as an aid to interpreting experimental results. The correction for spin-orbit splitting assumes that the radial matrix elements [Eqs. (4) and (5)] are insensitive to the energy splitting.

All of our results for inner subshells show good agreement between HF-L and HF-V, as seen from the tables, and, in general, with HS as well. This indicates, but by no means proves, that these inner-shell cross sections are probably fairly reli-

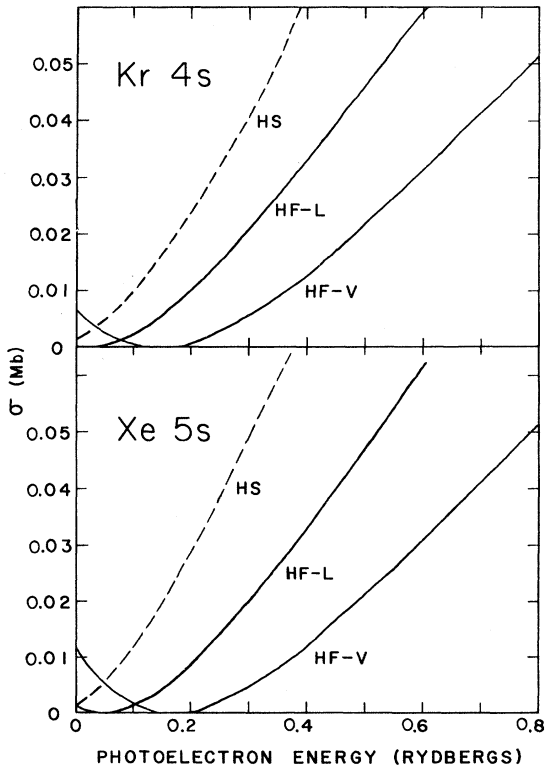

FIG. 10. Low-energy region of Kr $4s$ and Xe $5s$ subshell photoionization cross sections.

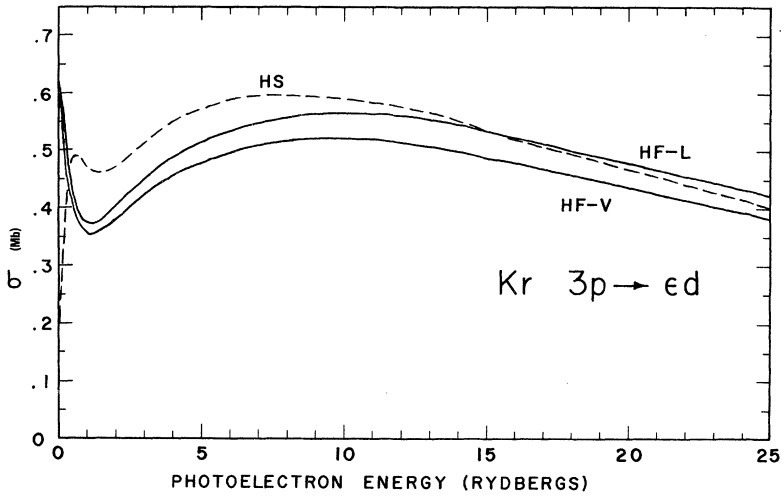

FIG. 11. Kr $3p \rightarrow \epsilon d$ partial photoionization cross section.

able. It is interesting to note, however, that in all cases HF-L lies above HF-V except for the Ar $2s \rightarrow \epsilon p$ transition near threshold.

3. $l \rightarrow l-1$ *Transitions*

The noteworthy feature of the $l \rightarrow l-1$ transitions is that for all subshells, both inner and outer, HF-L and HF-V agree to within a few percent, and HS is generally no further off. This confirms what many have thought to be the case[27,29,30] but, so far as we know, our results are the first extensive evidence of this. The agreement, further, tends to give confidence in the accuracy of the $l \rightarrow l-1$ cross sections.

4. *Connection with Intrachannel Coupling*

We can explain the various facets of the behavior of the HF cross sections within the framework of the intrachannel coupling of the Fano continuum configuration-interaction formalism[15,16] using the well-understood HS results as a starting point. In this theory, the HF continuum function of energy E, $|\psi_E\rangle$, is expanded in a basis of HS functions $|\epsilon\rangle$ (continuum *plus* discrete) using the reaction matrix $K(E)$

$$|\psi_E\rangle = \left(|E\rangle + P\int d\epsilon\, |\epsilon\rangle \, \frac{K_{\epsilon,E}}{E-\epsilon} \right) [1+\pi^2 K_{E,E}^2]^{-1/2} , \tag{14}$$

with P the principal-value integral and $K_{\epsilon,E} = \langle \epsilon | K(E) | E \rangle$ which satisfies

$$K_{\epsilon,\epsilon'} = V_{\epsilon,\epsilon'} + P\int d\epsilon''\, V_{\epsilon,\epsilon''} K_{\epsilon'',\epsilon'}/(E-\epsilon'') , \tag{15}$$

where V is the difference between the actual Ham-

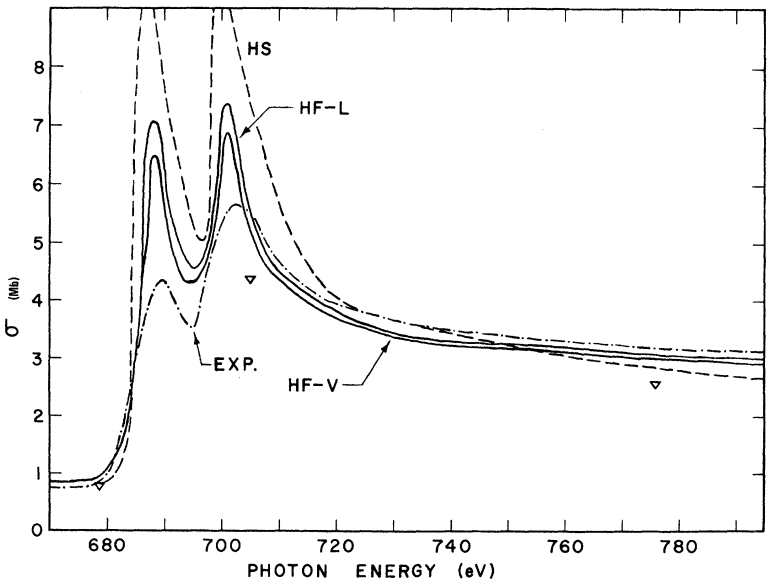

FIG. 12. Total photoionization cross section of Kr in the vicinity of the $3d(M_{4,5})$ threshold. Experimental data: dot-dash line, Ref. 28; triangles, Lukirskii *et al.*, Fig. 1.

iltonian and the HS-model Hamiltonian so that it amounts to the HF exchange potential minus the HS exchange. The HF photoionization matrix elements, at continuum energy E, is then given, in the length formulation, by

$$R_E^{\mathrm{HF-L}} = \left(R_E^{\mathrm{HS}} + P\int d\epsilon\, R_\epsilon^{\mathrm{HS}}\, \frac{K_{\epsilon,E}}{E-\epsilon}\right)[1+\pi^2 K_{E,E}^2]^{-1/2} \tag{16}$$

and in the (modified) velocity formulation by

$$R_E^{\mathrm{HF-V}} = \left(R_E^{\mathrm{HS}} + P\int d\epsilon\, R_\epsilon^{\mathrm{HS}}\, \frac{\epsilon-\epsilon_{nl}}{E-\epsilon_{nl}}\,\frac{K_{\epsilon,E}}{E-\epsilon}\right) \times[1+\pi^2 K_{E,E}^2]^{-1/2}, \tag{17}$$

R_E^{HS} being the HS matrix element at energy E and ϵ_{nl} the ionization energy of the photoelectron. Note that the appearance of the factor $(\epsilon-\epsilon_{nl})/(E-\epsilon_{nl})$ in the velocity matrix element means that length and velocity *must* differ when only the final-state wave function is improved.

The exchange potential in the noble gases is generally repulsive so that V is repulsive and its diagonal matrix element is positive. Since the matrix element $V_{\epsilon,\epsilon'}$ is a continuous function of the energy, it will then be positive for a range of energies with ϵ near ϵ'. Then, from Eq. (15), $K_{\epsilon,\epsilon'}$ will be positive for a range of energies around the diagonal. As in second-order perturbation theory the energy denominator greatly enhances the mixing coefficient for the wave function, Eq. (14), and photoionization matrix elements, Eqs. (16) and (17), for ϵ close to E so that, apart from an over-all normalization factor, the difference in matrix element between HF and HS is largely the effect of configuration interaction with nearby levels.

At the Cooper minimum, for example, where the HS matrix element vanishes, the interaction for $\epsilon < E$ has a positive energy denominator with a negative R_ϵ^{HS} so that its contribution is negative, while for $\epsilon > E$, R_ϵ^{HS} is, of course, positive and the energy denominator negative so its contribution is negative also. Thus the HF matrix element is negative so it has not yet reached the Cooper minimum. Hence, the Cooper minimum moves out to greater energy. The extra factor in the velocity matrix element enhances the contribution for $\epsilon > E$ but diminishes the $\epsilon < E$ effect so that, since the HS matrix element is much larger below the minimum than above, the $R_E^{\mathrm{HF-V}}$ is not quite as large (in magnitude) as $R_E^{\mathrm{HF-L}}$, and it will reach the minimum at a lower energy. This is borne out by all of our results for transitions where Cooper minima occur, Ar $3p \to \epsilon d$ (Fig. 6), Kr $4p \to \epsilon d$ (Fig. 7), Xe $5p \to \epsilon d$ (Fig. 8), and Xe $4d \to \epsilon f$ (Fig. 9). In the threshold region, most of the interaction is with $\epsilon > E$, since for these transitions very little of the oscillator strength is in the discrete so that the total effect

TABLE IV. Hartree-Fock results for the photoionization cross sections, in Mb, for individual subshells in Xe, as a function of the photoelectron energy in Xe, as a function of the photo electrons energy ϵ, in Ry. HF-L and HF-V refer to calculations in the length and velocity formulations.

	5p		5s		4d		4p		4s		3d		3p		3s	
ϵ(Ry)	HF-L	HF-V	HF-L	HF-V	HF-L	HF-V	HF-L	HF-V	HF-L	HF-V	HF-L	HF-V	HF-L	HF-V	HF-L	HF-V
0	5.77+1	3.74+1	1.13−3	1.21−2	1.31	1.23	5.09−1	4.69−1	1.81−1	1.67−1	6.61−2	6.53−2	7.46−1	7.38−1	8.19−2	8.05−2
0.5	5.69+1	3.49+1	6.25−2	1.85−2	1.26	1.05	4.64−1	4.30−1	1.94−1	1.78−1	3.95	3.29	7.72−1	7.51−1	8.70−2	8.65−2
1.0	3.19+1	1.48+1	1.11−1	6.95−2	1.23+1	8.77	4.43−1	4.06−1	1.92−1	1.76−1	7.64	6.86	3.71−1	3.67−1	8.53−2	8.37−2
1.5	1.82+1	7.34	1.50−1	1.03−1	1.98+1	1.34+1	4.33−1	3.92−1	1.90−1	1.73−1	4.40	3.95	3.65−1	3.59−1	8.34−2	8.18−2
2.0	1.03+1	3.72	1.70−1	1.22−1	2.44+1	1.59+1	4.30−1	3.90−1	1.87−1	1.70−1	3.49	3.13	3.66−1	3.60−1	8.15−2	7.99−2
3.0	3.78	1.13	1.83−1	1.35−1	2.84+1	1.72+1	4.34−1	3.83−1	1.82−1	1.64−1	2.76	2.47	3.67−1	3.60−1	7.89−2	7.71−2
4.0	1.56	4.60−1	1.79−1	1.31−1	2.27+1	1.26+1	4.40−1	3.84−1	1.78−1	1.60−1	2.48	2.22	3.64−1	3.57−1	7.77−2	7.58−2
6.0	4.45−1	1.76−1	1.54−1	1.10−1	6.33	2.84	4.47−1	3.85−1	1.71−1	1.52−1	2.25	2.00	3.59−1	3.51−1	7.64−2	7.44−2
8.0	2.07−1	1.20−1	1.24−1	8.71−2	1.07	3.98−1	4.43−1	3.80−1	1.59−1	1.40−1	2.10	1.87	3.55−1	3.46−1	7.46−2	7.25−2
10.0	1.37−1	9.88−1	1.00−1	6.94−2	2.54−1	2.57−1	4.32	3.68−1	1.46−1	1.28−1	2.02	1.79	3.46−1	3.37−1	7.28−2	7.06−2
15.0	7.86−1	7.31−1	6.27−2	4.42−2	5.94−1	6.47−1	3.90−1	3.32−1	1.21−1	1.05−1	1.84	1.60	3.28−1	3.18−1	6.83−2	6.59−2
20.0	5.80−1	5.80−1	4.48−2	3.15−2	8.13−1	7.44−1	3.43	2.91−1	1.02−1	8.78−1	1.66	1.44	3.08−1	3.00−1	6.43−2	6.19−2
30.0	4.08−1	3.87−1	2.61−2	1.81−2	7.48−1	6.05−1	2.60−1	2.20−1	7.28−1	6.22−1	1.33	1.13	2.71−1	2.60−1	5.67−2	5.43−2

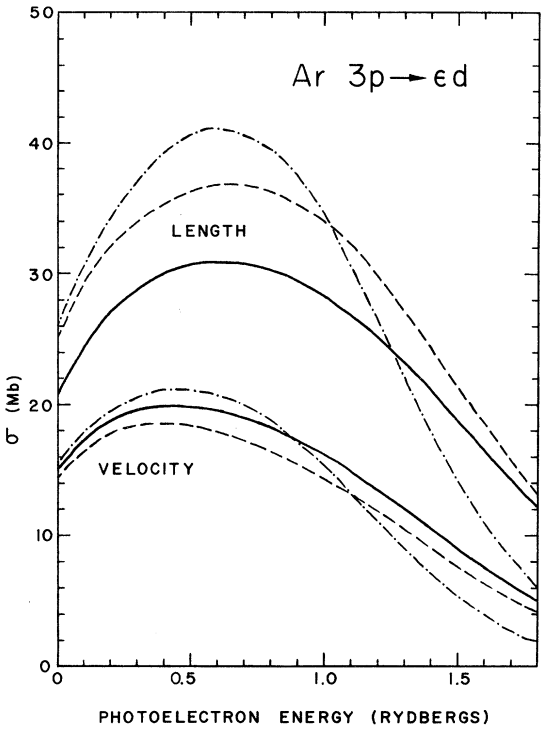

FIG. 13. Ar $3p \rightarrow \epsilon d$ photoionization cross section; using HS orbitals, dot-dash line; using HF Ar orbitals, dashed line; using HF Ar^+ orbitals and taking dipole matrix element with Ar $3p$ orbital, solid line.

on velocity is greater than on length. However both R_ϵ^{HS} *and* the energy denominator are negative and $K_{\epsilon,E}$ is positive, which make the contribution positive, which partially cancels the negative R_E^{HS}. Since the effect is greater for velocity than length, we expect $R_E^{HF\text{-}L}$ to be larger than $R_E^{HF\text{-}V}$ near threshold, for the above transitions, which is indeed the case.

For inner shells, as well as $l \rightarrow l-1$ transitions, most of the oscillator strength is in the discrete. Then, since for $\epsilon < E$ the contribution is positive and enhanced for length over velocity, the positive HS matrix element is increased more for length than velocity. This shows that in these cases length will generally be larger than velocity, which our results show. These arguments are not exact since occasionally $K_{\epsilon,E}$ can be negative, and we have omitted consideration of ϵ far from E. Thus, in certain cases velocity may be larger than length, but not very often and not by very much. We find this behavior for Ar $2s \rightarrow \epsilon p$ alone among inner shells.

5. *Comparison with Other Calculations*

There has been, in the past, no unanimity on what constitutes a Hartree-Fock calculation. There have been two difficulties; First, various possible choices can be made for the potential in which to solve for the final continuum state, as discussed in Sec. II. Second, the complexity of the HF equation for a continuum orbital is such that numerical errors can crop up fairly easily.

As to the first point, Fig. 13 shows the results of three different HF calculations for the Ar $3p \rightarrow \epsilon d$ transition; the ϵd wave function being solved for self-consistently with complete exchange in the residual ion field of HS orbitals, HF Ar^0 orbitals, and HF Ar^+ orbitals. The HF-V curves are in fairly good agreement with each other, while there are moderately large differences among the HF-L results indicating that the various approximations are substantially the same at intermediate distances from the nucleus but much less so at the outer edge of the atom. For these reasons, then, the agreement among the several approximations will be better for inner shells for which the details of the outer edge of the atom are less important.

Concerning numerical accuracy, we have performed a number of checks in an effort to be sure our work was free of numerical blunders. We varied the integration range and mesh size by more than a factor of 2 and found differences in calculated cross sections and wave functions of less than 0.1%. We calculated the photoionization matrix elements at each iteration of the self-consistent-field calculation to ensure that they converged completely. Our HF equations were checked against those reported by other workers. An error was found in an equation given in a Ne calculation,[31] but it is unclear whether this was a typographical error or a real error in the calculation.

Finally, we have compared our results for the Ar $3p$ photoionization with the continuum orbital in the field of Ar^+ HF functions to a similar calculation by Lipsky and Cooper.[32] The Lipsky-Cooper results are actually from a close-coupling calculation, but the coupling has almost no effect.[32] This comparison is shown in Fig. 14, where it is seen that the two calculations give essentially exactly the same results. This convinces us that our results are free of numerical blunders.

Comparison between our HF results using HS orbitals for the residual ion field and the calculations of Starace,[30] who actually performed an *intrachannel* calculation starting with a HS basis, is shown in Fig. 15 for the Ar $3p \rightarrow \epsilon d$ transition and in Fig. 16 for Xe $4d \rightarrow \epsilon f$. Formally, the two methods are exactly equivalent; differences can be ascribed only to numerical errors in one (or both) of the calculations. The comparisons show excellent agreement near threshold but substantial disagreements at photoelectron energies of a rydberg and higher. A possible reason for this is the energy cutoff introduced by Starace in solving the integral equations for the K matrix; neglect of the energies

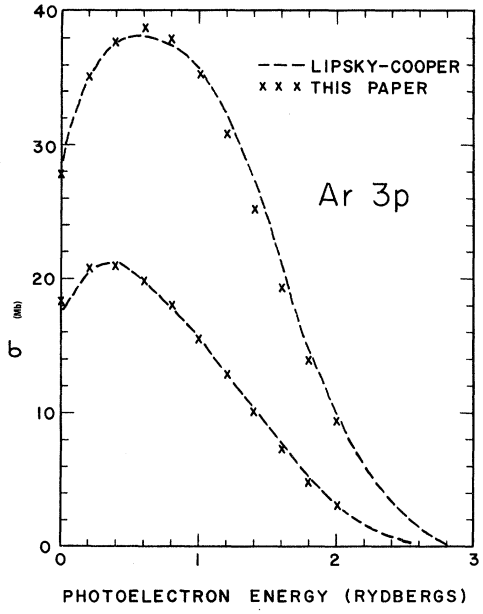

FIG. 14. Ar $3p$ photoionization cross section; close-coupling results of Ref. 32, dashed line; results of HF calculation using Ar^+ HF field and taking dipole matrix element with Ar $3p$ HF orbital, solid line.

above the cutoff would almost certainly affect the matrix elements at the higher energies more than the lower ones near threshold because of the energy denominator in Eq. (14). Attempts to increase the cutoff energy, by as much as a factor of 2, have not changed the intrachannel results by any appreciable amount, however.[33] It may be that one must include a significant portion of the channel for numerical accuracy. In any case, we feel that in view of this, it is probably best to carry out *inter*-channel coupling starting with HF functions, i.e., with each channel diagonalized, as suggested by Altick.[34]

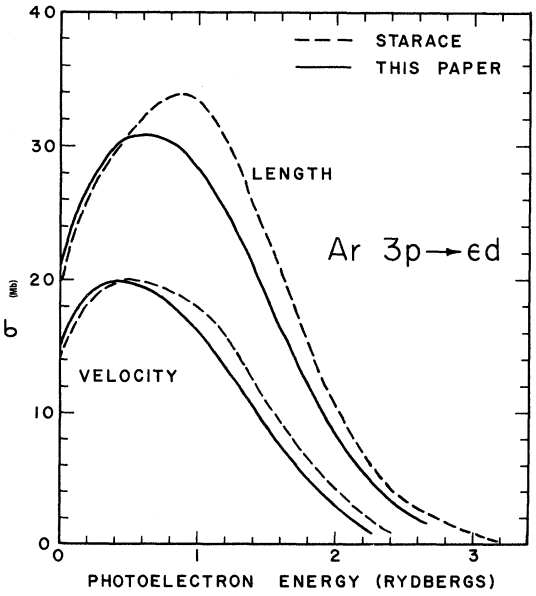

FIG. 15. Ar $3p \rightarrow \epsilon d$ photoionization cross section; using HS orbitals, solid line; results of Ref. 30, dashed line.

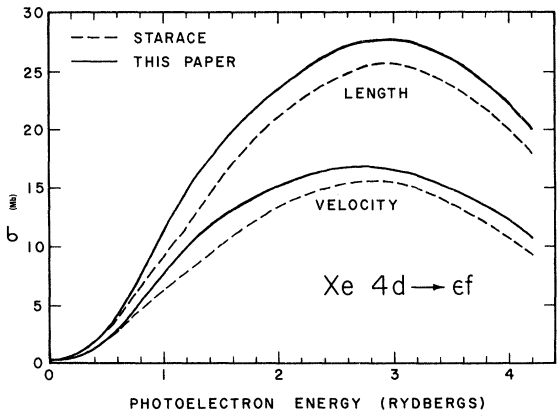

FIG. 16. Xe $4d \rightarrow \epsilon f$ photoionization cross section; using HS orbitals, solid line; results of Ref. 30, dashed line.

IV. ANGULAR DISTRIBUTION OF PHOTOELECTRONS

The asymmetry parameter $\beta(\epsilon)$ which determines the angular distribution of photoelectrons [Eqs. (6) and (7)], is a function of the photoionization matrix elements and of the continuum-wave phase shifts, given by Eq. (8). Physically, the nature of the angular distribution of the photoelectrons is determined by the angular structure of the continuum wave function representing the ejected electron. For initial s electrons there is only a single final channel, a p wave, so the angular distribution does not vary with energy, β always being equal to 2. For electrons with nonzero initial angular momentum, l say, there are two allowed channels $l \pm 1$ which can interfere, and since the electron amplitude in the two allowed channels varies with energy, the interference, and thus the asymmetry, will also change with energy. Such changes can be characterized by variation of the difference in phase shifts with energy. Before turning to a discussion of $\beta(\epsilon)$ then, it is of interest to investigate the calculated phase shifts.

A. Phase Shifts

The phase shifts of the continuum wave functions (with respect to Coulomb waves) are plotted in Figs. 17–20. The s- and p-wave phase shifts decrease monotonically from their threshold values (Figs. 17 and 18) while the d- and f-wave phase shifts are increasing at threshold as seen in Figs. 19 and 20. The general behavior of the phase

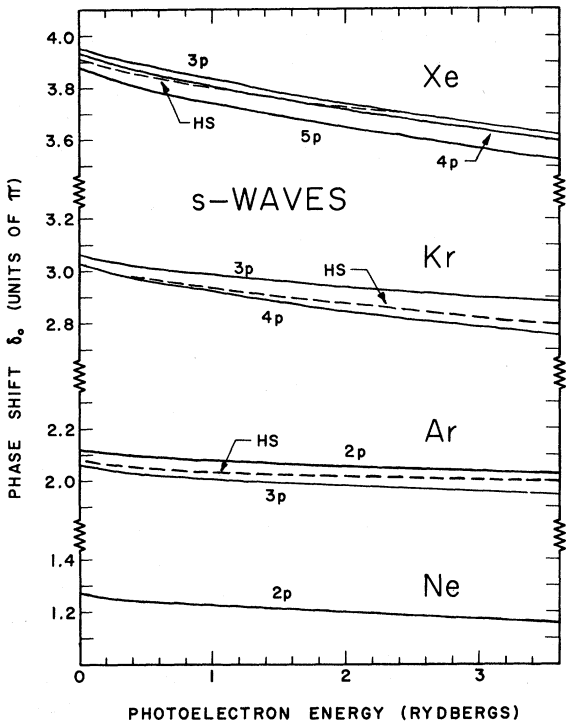

FIG. 17. s-wave phase shifts (Ne HS values identical with HF values).

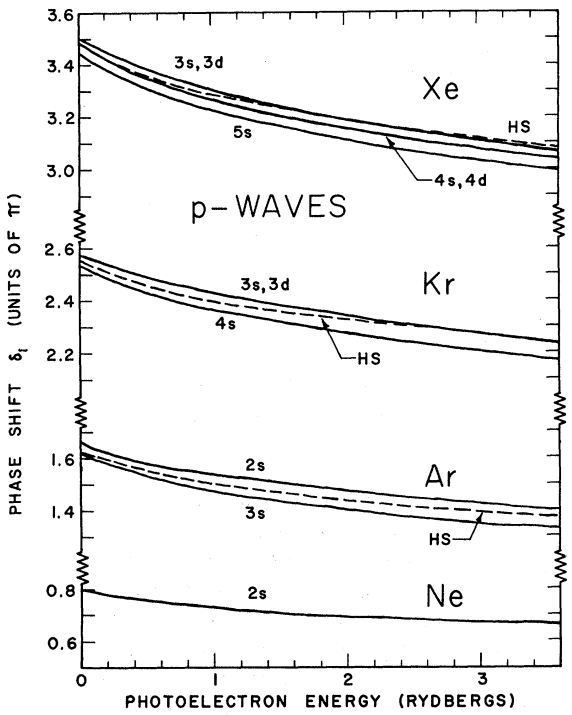

FIG. 18. p-wave phase shifts (Ne HS and HF values identical as are HF values for initial s or d electrons).

shifts, as a function of the continuum electron energy has been examined previously in detail in terms of the HS potential.[35] The large centrifugal barrier seen by d and f waves prevents these continuum wave functions from penetrating appreciably to the inner regions at small energies, and thus the phase shift remains small until sufficient energy is available to the electron to enable it to surmount the centrifugal potential barrier. At low energies, due to this barrier, the d- and f-wave phase shift behavior will reflect the large-r behavior of the potential, while the behavior at large energies reflects the small-r nature of the potential. For s and p waves, which are very penetrating, all parts of the potential are important at both small and large energies. From Figs. 17–20 it is seen that in most cases, the phase shifts found, assuming that the photoelectron moves in the HS field, tend to agree at low energies with the phase shifts from the HF calculation on ionization of an outer-shell electron, but at high energies they agree with the phase shifts from the HF inner-shell ionization results, indicating that the HS potential in the outer region of the atom is fairly close to the HF with an *outer* shell hole, while in the intermediate region it more nearly approximates the HF with a vacancy in an *inner* shell. It is of interest to note that, in the HF approximation, the p-wave phase shifts with a vacancy in a given shell are the same irrespective of whether this vacancy is in an s or d subshell.

The accuracy of our computed phase shifts is

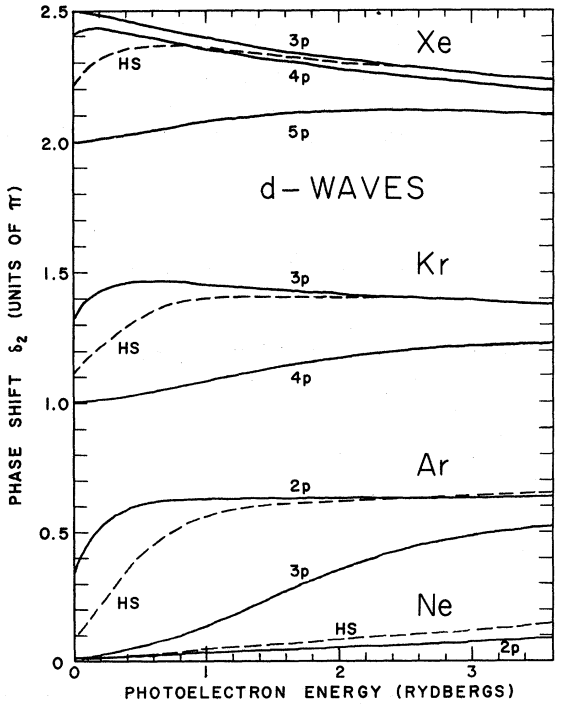

FIG. 19. d-wave phase shifts.

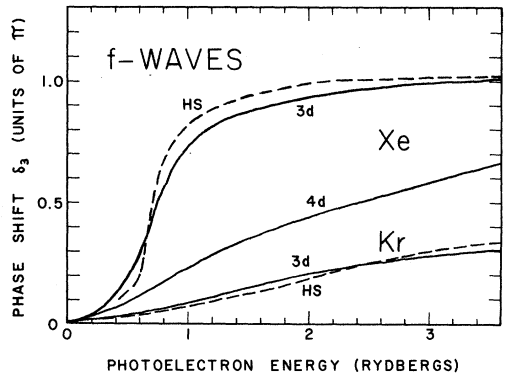

FIG. 20. f-wave phase shifts.

limited by the fact that we have not included two important effects in the theoretical treatment: coupling of the final states (essentially a close-coupling problem) and deviations from LS coupling due to the spin-orbit Hamiltonian. These effects have been investigated recently in xenon by Lu and Fano[36,37] and were found to be of considerable importance; coupling between channels is strong, and LS coupling to a great extent breaks down. This is also evidenced by the fact that the states leading up to the outer $p^{1/2}$ and $p^{3/2}$ ionization thresholds in xenon have rather different experimental binding energies[38,39] with respect to their respective thresholds, indicating differing wave functions and mixing between ^1P and ^3P levels. Our treatment does not consider spin-orbit effects so we get no such differences. These experimental energy differences[39,40] are quite small (but increasing with increasing Z) for neon, argon, and krypton, which is not unexpected in view of the Z^4 dependence of spin-orbit effects. Thus, we expect the mixing to be important for Xe but not for the others. A further indication of the lack of triplet-singlet mixing in Ne and Ar comes from transition probability measurements[41,42] which find only one optically allowed state of the above type, the ^1P, rather than the two one would find if there were significant mixing. This has important implications for the accuracy of our angular distributions which shall be discussed later.

B. Angular Distributions: Asymmetry Parameters

The asymmetry parameters β describing the angular distributions found in the HF-L, HF-V, and HS approximations are shown in Figs. 21–27.

For inner p subshells, Ar $2p$ (Fig. 21), Kr $3p$ (Fig. 22), and Xe $3p$, $4p$ (Fig. 23), it is seen that the β's all have essentially the same energy dependence, falling rapidly from their threshold values to a minimum at a photoelectron energy of about 8 eV, and then rising slowly to a constant value of approximately 1.5 in all cases. Although β depends both on the ratio of the dipole matrix elements in the two allowed channels and on the phase shifts, it is found, on examination, that the matrix-element ratio varies only slowly with energy. Thus most of the energy dependence of β is carried by the cosine term in Eq. (8), and the variation in β is due mainly to the variation of the phase shifts with energy. In the near-threshold region the changes in the phase shifts with energy arise largely from the changes in the Coulomb phase shifts $\sigma_{l\pm1}$ rather than the $\delta_{l\pm1}$. At high energies, since the matrix elements $R_{l\pm1}$ each fall off with photoelectron energy ϵ as $\epsilon^{-(2l+9)/4}$, where l is the angular momentum of the initial state, and since the phase-shift difference remains nearly constant, β approaches essentially a constant value.

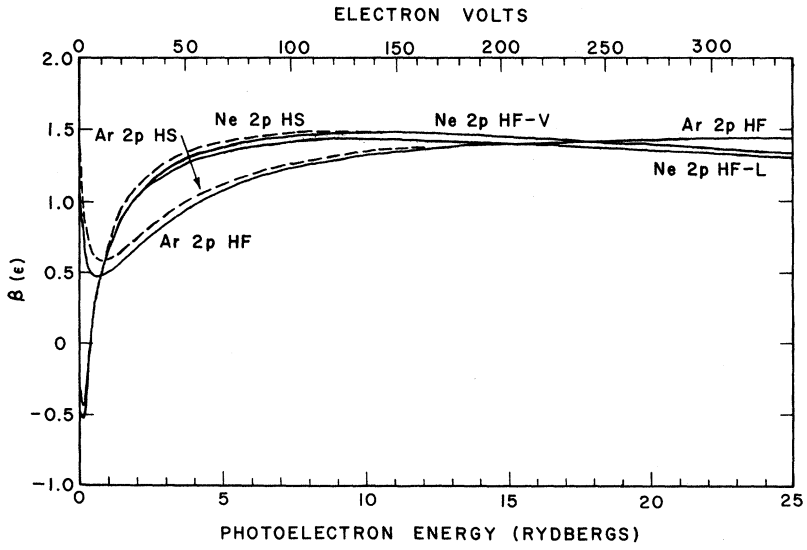

FIG. 21. Asymmetry parameter β, for electrons ejected from Ne and Ar $2p$ subshells (Ar $2p$ results identical in HF-L and HF-V formulations).

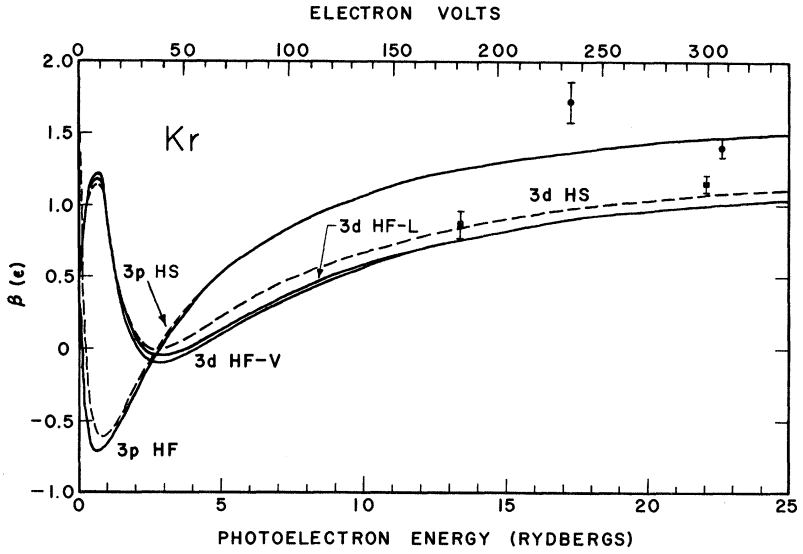

FIG. 22. Asymmetry parameter β, for electrons ejected from Kr $3p$ and $3d$ subshells (Kr $3p$ results identical in HF-L and HF-V formulations).

The asymmetry parameter for the Ne $2p$ subshell, shown in Fig. 21, resembles more closely the inner p subshells of Ar, Kr, and Xe, than the outer p subshells of these atoms. This behavior of the $2p$ subshell of Ne was noted earlier in the discussion of subshell cross sections. Compared to the $2p$ subshell β in Ar the minimum in the Ne $2p$ asymmetry parameter is sharper and occurs nearer threshold, at about 3 eV.

It is noteworthy that for the inner p subshells, as well as for the Ne $2p$, the β's calculated in the length and velocity HF approximations are almost exactly the same and also in very good agreement with HS results, despite non-negligible (although small) differences among the cross sections predicted by the various approximations. This is a consequence of the fact that the expression for β [Eq. (8)] is a ratio so that the effect of even a substantial change in the cross section is largely cancelled out. Further, the HF phase shifts in these cases are substantially the same as the HS seen in Figs. 21 and 23.

The β's for the $3p$ shell of Ar, $4p$ of Kr, and $5p$ of Xe are shown in Figs. 24, 25, and 26, respectively. They differ from the inner p-shell β's in two important respects. First, in the near-threshold region they increase as the photoelectron energy increases giving rise to a maximum rather than a minimum; second, they exhibit a second turning point at higher energies, at about 50 eV in Ar, 80 eV in Kr, and 90 eV in Xe. Although the first maximum is due mainly to the variation of the Coulomb

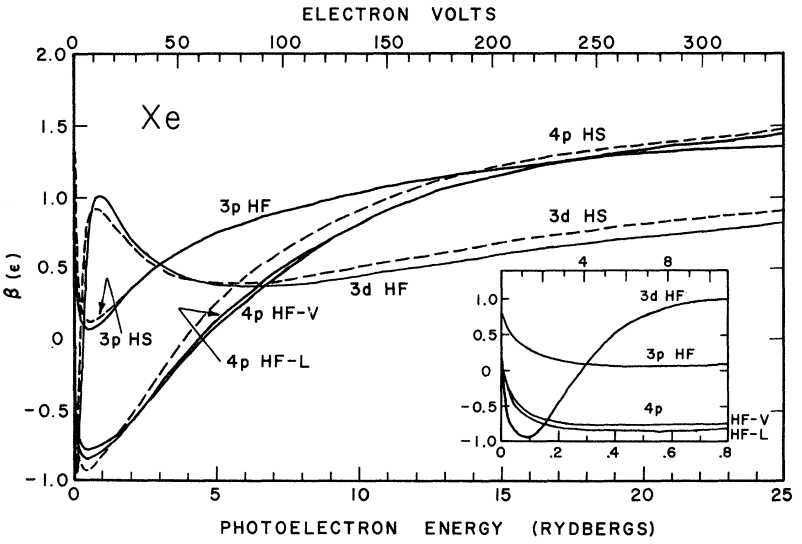

FIG. 23. Asymmetry parameter β, for electrons ejected from Xe $4p$, $3d$, and $3p$ subshells (Xe $3p$ and $3d$ results identical in HF-L and HF-V formulations).

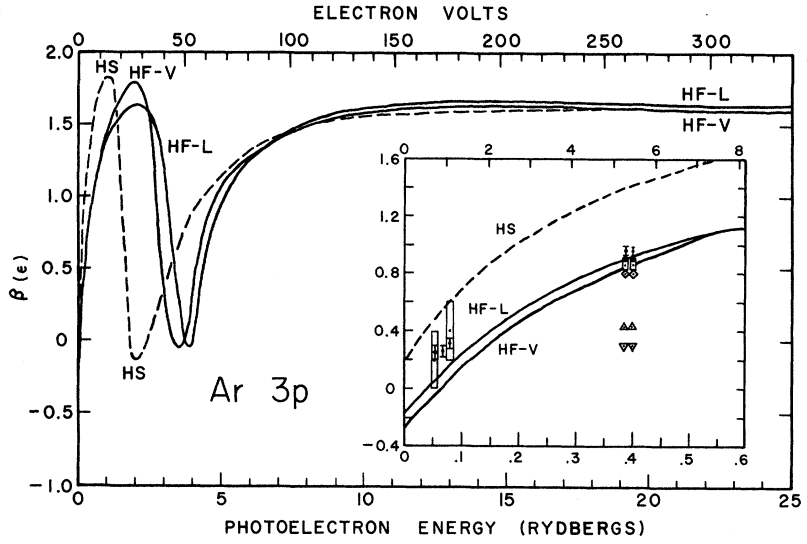

FIG. 24. Asymmetry parameter β, for electrons ejected from Ar $3p$ subshell. In the low-energy region, data points shown are ⧫ Ref. 13; ◇ Ref. 11; △ Ref. 8; ▽ Ref. 5; ⊡ Ref. 14.

phase shifts with energy, the increasing behavior of β near threshold is a consequence both of an increasing cosine term and of the fact that for these outer p subshells the ratio of the dipole matrix elements is negative below an energy of about 50 eV. The δ_{l+1} phase shifts are varying far more rapidly with energy for outer p subshells, than for inner, tending to further enhance the oscillatory behavior of the β's. Further rapid variations of β with energy are also caused by the change in sign of the d-channel matrix element (indicated by the existence of a Cooper minimum in each of these cases) which changes the sign of the cosine term. Experimental confirmation of this oscillatory behavior would be very desirable.

The β's for these outer p subshells show remarkable agreement among the various approximations despite the rather different cross sections each predicts (Figs. 6–8). Some differences show up because the Cooper minimum, where β for p shells goes through a zero, occur at a different energy in each approximation; these differences get progressively greater from Ar to Xe since these energies become more widely separated. Nevertheless, except for this energy shift, even the results in the simple HS model are quite good.

The asymmetry parameter for these outer p shells also tends towards a value of about 1.5 at the very large energies, similar to the inner-shell behavior. This is a consequence of the fact that, at the higher energies, the argument of the cosine term in Eq. (8) is such that the cosine itself is

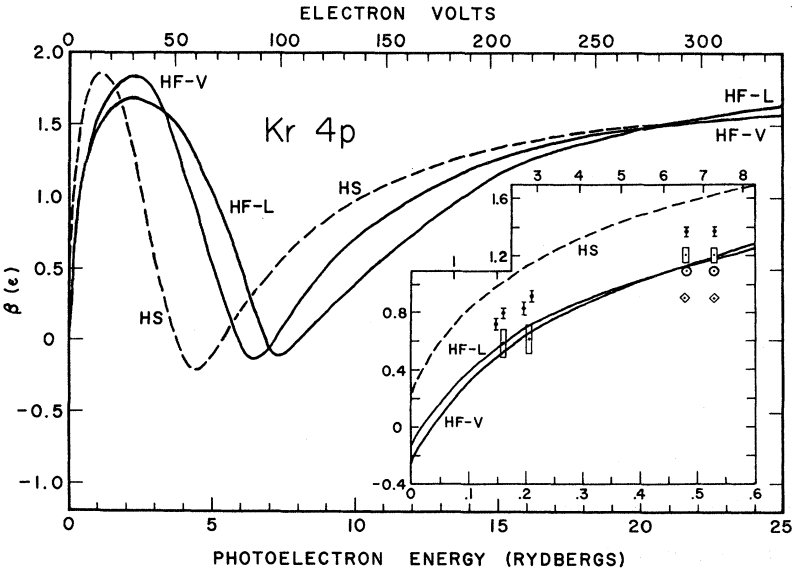

FIG. 25. Asymmetry parameter β, for electrons ejected from Kr $4p$ subshell. In the low-energy region, data points shown are ⧫ Ref. 13; ⊙ Ref. 6; ◇ Ref. 12; ⊡ Ref. 14.

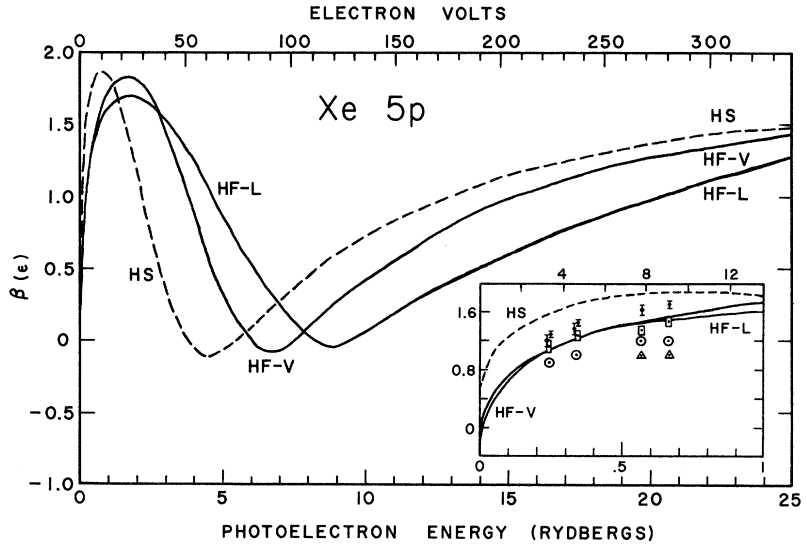

FIG. 26. Asymmetry parameter β, for electrons ejected from the Xe $4p$ subshell. In the low-energy region, data points shown are ⧫ Ref. 13; ⊙ Ref. 6; △ Ref. 8; ⊡ Ref. 14.

about -1 for all the p subshells. This is very different from the hydrogenic behavior which gives about zero for the argument of the cosine term at high energies and predicts a β quite close to zero as well.

The asymmetry parameters for Kr $3d$ and Xe $3d$ are shown in Figs. 22 and 23, respectively. They both vary somewhat more rapidly with energy near threshold than do the p-subshell results, which is attributable to the fact that the ratio of the dipole matrix elements vary somewhat more rapidly with energy than do the p-subshell ratios; the $3d$ β's will not follow the oscillation of the cosine term quite so closely. Nevertheless, the sharp change in β near threshold is due principally to the change in Coulomb phase shifts. It is also seen that the β's calculated in the HF-L, HF-V, and HS approximations show excellent agreement with each other, just as for the inner p subshells.

The asymmetry parameter for Xe $4d$ is shown in Fig. 27 where the outstanding feature is the extremely oscillatory nature of β as a function of energy. This phenomenon has been reported previously, [43] but only using the HS approximation; the HF results are seen to be *qualitatively* the same, the energy shift in the intermediate region being due to the differing locations of the Cooper minimum, as discussed in connection with outer p shells. The agreement among all the approximations, especially in the threshold region, is all the more remarkable in view of the large discrepancies in the cross sections they predict.

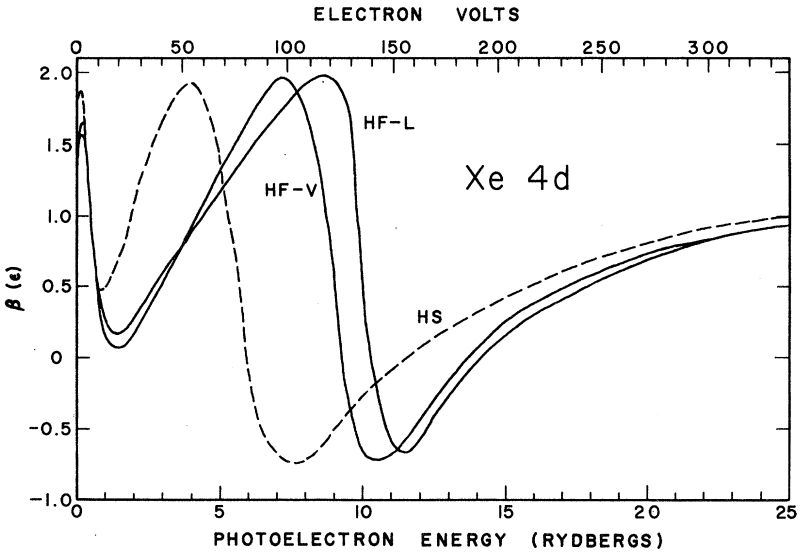

FIG. 27. Asymmetry parameter β, for electrons ejected from the Xe $4d$ subshell.

The oscillations in the asymmetry parameter follow closely the oscillations of the cosine term in the expression for β [Eq. (8)], whose argument changes by $\sim \frac{5}{2}\pi$ from threshold to 8 Ry in the HF approximation. For the first rydberg above threshold the variation is due mainly to the Coulomb phase shifts; from 1 to 8 Ry it is due mostly to the shape resonance in the f-wave channel. Above 8 Ry, the only major variation of β with energy occurs principally because of the Cooper minimum and the associated change in sign of R_{l+1}. An experimental study of this case would be extremely desirable.

C. Comparison with Experimental $\beta(\epsilon)$'s

Recently there have been a number of experimental determinations of the angular distributions of electrons arising from the photoionization of the noble gases.[4-8,11-14] In general these experiments have confirmed that the angular dependence of the photoelectron spectrum is given correctly by Eq. (7). But so far there have not been measurements over a sufficiently large energy range to determine the over-all energy dependence of the asymmetry parameter β. The measurements in the noble gases that have been reported[4-8,11-14] have, except for one, been concerned only with the outer shells of Ar, Kr, and Xe. These points are shown in the inserts in Figs. (24), (25), and (26), respectively.

The experimental points show a considerable scatter but the more recent measurements of Morgenstern *et al.*,[12] Vilesov and Lopatin,[11] and Carlson and Jonas[14] do tend to agree with each other and with the theoretical results.

The data of Morgenstern *et al.* is the most extensive available, and in all cases it lies between the results of the HS calculation and the HF calculation, in general somewhat closer to the HF. While most of the experimental data confirm that the anisotropy of the photoelectrons increases with increasing photoelectron energy in the near-threshold region, the data of Refs. 12 and 14 appear to reproduce the exact shape of the $\beta(\epsilon)$ curves for the $3p$, $4p$, and $5p$ subshells of Ar, Kr, and Xe, respectively. As β varies quite rapidly at small energies, due to the fairly rapid change in the phase shifts, it is possible that at a given energy value, the present theory would predict a value of β that is substantially different from the experimental value, due to differences between the experimental and theoretical thresholds. It would be of great value, therefore, if the experimental data were extended beyond the threshold region and the energy dependence of β determined over a wide range of photoelectron energies.

In Kr, Krause[4] has determined β for photoelectron energies from several hundred eV to the keV range for $3p$ and $3d$ subshells. At fairly high energies ($\gtrsim 200$ eV) there is satisfactory agreement between theory and the data of Krause for the $3p$ and $3d$ subshells, as seen in Fig. 22, and in particular the data reproduce the high-energy trend of the theoretical values. We have shown only the data points below 25 Ry. Higher-energy experimental values of β have been found by Manson and Cooper[27] to be in agreement with the HS results which are remarkably close to the HF results.

At this point it is worthwhile to consider, from a theoretical viewpoint, the accuracy of the calculated β's since there are not yet enough reliable experimental data to provide a reasonable assessment. As has been shown, the β's are rather insensitive functions of the details of the radial wave functions. Thus, as long as the conditions for which the expression for β [Eq. (8)] was derived, e.g., LS coupling and the dipole approximation, hold, it is expected that our β's will be fairly accurate. On the other hand, when LS coupling breaks down, our expression for β will not necessarily be correct. If the deviation from LS coupling is small, it is reasonable to suppose that the expression for β will still be a good approximation. As we discussed in connection with quantum defects, this is the case for Ne, Ar, and Kr. In Xe, however, the deviation is significant, so that the β's predicted for Xe may be only a zeroth approximation, although the available experimental data show no strong evidence of such a deviation.

Some attempt has been made experimentally to distinguish between the asymmetry parameters describing photoelectrons that leave the ion in different spin-orbit states in atoms other than noble gases. While one set of experimental results on Cd[9] indicates that an LS-coupled model does not describe the observed angular distribution of photoelectrons, observations by the same experiments on Hg,[10] which is much heavier and should show even further deviations from LS coupling, fail to show any effect of this in the β's of the two states split by the spin-orbit interaction. Further work on this matter is in progress.

V. CONCLUSIONS

Sections I–IV indicate substantial agreement between experimental photoabsorption cross sections and the theoretical Hartree-Fock results presented in this paper, except in the regions just above the Ar $3p$, Kr $4p$, and Xe $4d$ and $5p$ thresholds; HF-length and HF-velocity cross sections are also in good agreement in all but these energy ranges. Many interesting features of the individual subshell cross sections, which do not appear in the total photoabsorption measurements because they are sums over all energetically accessible subshells, have been emphasized, since the possibility now exists of investigating such features, unhampered by the background of the other subshells, via the

technique of photoelectron spectroscopy.

The angular distribution of photoelectrons and associated asymmetry parameter β which we calculated were found to be in good agreement with recent experimental work. Further, HF-length and HF-velocity calculations predict asymmetry parameters which are substantially the same, and even the HS results are in fairly good agreement indicating that large-scale calculations in the HS approximation would be useful. Such calculations are in progress. Unfortunately experimental data in the noble gases exist only in the threshold region ($\epsilon \leq 10$ eV) except for the M shell of Kr. In the intermediate energy region, where a rapid oscillatory behavior of the asymmetry parameter was found, no experimental work has been reported. Such measurements would be extremely useful, not only to compare with existing calculations but also to enable one to work backwards and determine experimentally the differences between the phase shifts in the two outgoing channels as well as the ratio of matrix elements in each.

Since this paper is aimed primarily at photoelectron spectroscopy, rather than total absorption cross sections, we have used a single-particle model of the atom. This makes the interpretation of the results in terms of individual subshells simple and unambiguous. Further, the expression which is employed for the asymmetry parameter [Eq. (8)] has been derived only for single-particle wave functions. While more sophisticated calculations, like those of Amusia *et al.*[17] for example, appear to yield better total cross sections, a further improvement in the theory of the angular distributions would involve an extension of Eq. (8) to multichannel or correlated wave functions.

APPENDIX

In this Appendix we present the exchange terms that were used in the solutions to the HF equation in order to allow others to check our calculations. In particular we give the form of $X(r)$, that appears in Eq. (12), for the various $nl' \rightarrow \epsilon l$ transitions, using the same notation as in Sec. II.

(i) For $n'p \rightarrow \epsilon s$,

$$X(r) = \sum_n Y^0(ns, \epsilon s) P_{ns} + \sum_n (1 - \tfrac{2}{3}\delta_{n',n}) Y^1(np, \epsilon s) P_{np} + \sum_n Y^2(nd, \epsilon s) P_{nd}\,; \tag{A1}$$

(ii) for $n'p \rightarrow \epsilon d$,

$$X(r) = \sum_n \tfrac{1}{5} Y^2(ns, \epsilon d) P_{ns} + \sum_n [(\tfrac{2}{5} - \tfrac{4}{3}\delta_{n',n}) Y^1(np, \epsilon d) + \tfrac{9}{35} Y^3(np, \epsilon d) P_{np}]$$
$$+ \sum_n [Y^0(nd, \epsilon d) + \tfrac{3}{7} Y^2(nd, \epsilon d) + \tfrac{2}{7} Y^4(nd, \epsilon d)] P_{nd}\,; \tag{A2}$$

(iii) for $n'd \rightarrow \epsilon f$,

$$X(r) = \sum_n \tfrac{1}{7} Y^3(ns, \epsilon f) P_{ns} + \sum_n [\tfrac{9}{35} Y^2(np, \epsilon f) + \tfrac{4}{21} Y^4(np, \epsilon f)] P_{np}$$
$$+ \sum_n [(\tfrac{3}{7} - 2\delta_{n',n}) Y^1(nd, \epsilon f) + \tfrac{4}{21} Y^3(nd, \epsilon f) + \tfrac{50}{231} Y^5(nd, \epsilon f)] P_{nd}\,; \tag{A3}$$

(iv) for $n'd \rightarrow \epsilon p$ and $n's \rightarrow \epsilon p$,

$$X(r) = \sum_n (\tfrac{1}{3} - \tfrac{2}{3}\delta_{n',n}\delta_{l',0}) Y^1(ns, \epsilon p) P_{ns} + \sum_n [Y^0(np, \epsilon p)] P_{np}$$
$$+ \sum_n [(\tfrac{2}{3} - \tfrac{4}{3}\delta_{n',n}\delta_{l',2}) Y^1(n'd, \epsilon p) + \tfrac{3}{7} Y^3(nd, \epsilon p)] P_{nd}\,. \tag{A4}$$

*Present address: School of Physical Sciences, New University of Ulster, Coleraine, Northern Ireland.

[1]J. H. Hubbell and M. J. Berger, Natl. Bur. Std. Rept. No. 8681, 1966 (unpublished).

[2]J. A. R. Samson, Advan. Atom. Mol. Phys. 2, 178 (1966).

[3]K. Siegibahn, C. Nordling, A. Fahlman, R. Nordberg, K. Hamrin, J. Hedman, G. Johansson, T. Bergmark, S. Karlsson, I. Lindgren, and B. Lindberg, Nova Acta Reg. Soc. Sci. Upsaliensis, Ser. IV 20, 1 (1967).

[4]M. O. Krause, Phys. Rev. 177, 151 (1969).

[5]J. A. R. Samson, Phil. Trans. Roy. Soc. London A268, 141 (1970).

[6]J. W. McGowan, D. A. Vroom, and A. R. Comeoux, J. Chem. Phys. 51, 5626 (1969).

[7]J. Berkowitz and H. Ehrhardt, Phys. Letters 21, 531 (1966).

[8]J. Berkowitz, H. Ehrhardt, and T. Tekaat, Z. Physik 200, 69 (1967).

[9]H. Harrison, J. Chem. Phys. 52, 901 (1970).

[10]H. Harrison, Bull. Am. Phys. Soc. 15, 1514 (1970).

[11]F. I. Vilesov and Z. N. Lopatin, Vestn. Leningr. Univ. Ser. Fiz. i Khim. 64 (1970).

[12]R. Morgenstern, A. Niehaus, and M. W. Ruf, Chem. Phys. Letters 4, 635 (1970).

[13]R. Morgenstern, A. Niehaus, and M. W. Ruf, in *Electronic and Atomic Collisions*, edited by L. Branscomb *et al.* (North-Holland, Amsterdam, 1971), p. 167.

[14]T. A. Carlson and A. E. Jonas, J. Chem. Phys. (to be published).
[15]U. Fano, Phys. Rev. 124, 1866 (1961).
[16]U. Fano and J. W. Cooper, Rev. Mod. Phys. 40, 441 (1968).
[17]M. Ya. Amusia, N. A. Cherepkov, and L. V. Chernysheva, Zh. Eksperim. i Teor. Fiz. 60, 160 (1971) [Sov. Phys. JETP 33, 90 (1971)].
[18]P. L. Altick and A. E. Glassgold, Phys. Rev. 133, A632 (1964).
[19]H. Bethe and E. Salpeter, *Quantum Mechanics of One- and Two-Electron Atoms* (Academic, New York, 1957), Sec. 69.
[20]A. F. Starace, Phys. Rev. A 3, 1242 (1971).
[21]J. Cooper and R. N. Zare, J. Chem. Phys. 48, 942 (1968).
[22]J. Cooper and R. N. Zare, in *Lectures in Theoretical Physics*, Vol. 11c, edited by S. Geltman, K. Mahanthappa, and W. Brittin (Gordon and Breach, New York, 1969), p. 317.
[23]J. W. Cooper and S. T. Manson, Phys. Rev. 177, 157 (1969).
[24]C. N. Yang, Phys. Rev. 74, 764 (1948).
[25]F. Herman and S. Skillman, *Atomic Structure Calculations* (Prentice-Hall, Englewood Cliffs, N. J., 1963).
[26]D. L. Ederer and D. H. Tomboulian, Phys. Rev. 133, A1525 (1964).
[27]S. T. Manson and J. W. Cooper, Phys. Rev. 165, 126 (1968).
[28]R. D. Deslattes, Phys. Rev. Letters 20, 483 (1968).
[29]J. Cooper, Phys. Rev. 128, 681 (1962).
[30]A. Starace, Phys. Rev. A 2, 118 (1970).
[31]K. G. Sewell, Phys. Rev. 138, A418 (1965).
[32]L. Lipsky and J. W. Cooper (private communication).
[33]A. Starace (private communication).
[34]P. L. Altick (private communication).
[35]S. T. Manson, Phys. Rev. 182, 97 (1969).
[36]K. T. Lu and U. Fano, Phys. Rev. A 2, 81 (1970).
[37]K. T. Lu, Phys. Rev. A 4, 579 (1971).
[38]C. E. Moore, *Atomic Energy Levels*, Natl. Bur. Std. No. 467 (U. S. GPO, Washington, D.C., 1949).
[39]R. P. Madden, D. L. Ederer, and K. Codling, Phys. Circ. Rev. 177, 136 (1969).
[40]K. Yoshino, J. Opt. Soc. Am. 60, 1220 (1970).
[41]W. L. Wiese, M. W. Smith and B. M. Glennon, *Atomic Transition Probabilities* (U. S. GPO., Washington, D.C., 1966), Vol. 1, NSRDS-NBS 4.
[42]W. L. Wiese, M. W. Smith, and B. M. Miles, *Atomic Transition Probabilities* (U. S. GPO., Washington, D.C., 1969), Vol. 2, NSRDS-NBS 22.
[43]S. T. Manson, Phys. Rev. Letters 26, 219 (1971).
[44]A. P. Lukirskii, I. A. Brytov, and T. M. Zimkina, Opt. i Spectroskopiya 17, 438 (1964) [Opt. Spectry. 17, 234 (1964)].

PHYSICAL REVIEW A VOLUME 5, NUMBER 1 JANUARY 1972

Distributions in Energy and Angle of Electrons Ejected from Molecular Hydrogen by 0.3–1.5-MeV Protons*

L. H. Toburen and W. E. Wilson
Battelle Memorial Institute, Pacific Northwest Laboratory, Richland, Washington 99352
(Received 12 July 1971)

Cross sections for the ejection of electrons, differential in electron energy and angle of emission, have been measured for energetic protons on molecular hydrogen. Electron-energy distributions are presented for ten angles between 20 and 130 deg for each of five proton energies between 0.3 and 1.5 MeV. The results are compared with calculations based on binary-encounter theory, the Born approximation, and the Faddeev equations. Qualitative agreement with the latter provides supporting evidence for the inclusion of a long-range electron-proton interaction in the collision theory for proton energies as high as 1.5 MeV.

I. INTRODUCTION

Measurements of cross sections, differential in electron energy and emission angle, for the ejection of electrons in ion-molecule collisions provide information concerning the ionization process. Comparison of these cross sections to theoretical ones is a test of the reliability and limitations of the theoretical treatments used to describe the ionization process and, hence, provides information concerning the relative importance of various types of interactions which enter into a complete description of ionization by fast charged particles. Several different theoretical approaches have been used to calculate double-differential electron-ejection cross sections[1–5] for incident protons. In general, the nature of these calculations restricts the range of validity of the results to apply to protons with velocities greater than several times the velocity of the electron in the first Bohr orbit of the hydrogen atom. Previous measurements of double-differential cross sections for ejection of electrons from molecular hydrogen were limited to protons with a maximum energy of 0.3 MeV,[5–7] in which case the velocity of the proton was only about 3.5 times the velocity of the electron in the first Bohr orbit of hydrogen. In our work, we have extended the proton energy range to 1.5 MeV in order to obtain cross sections which may be compared more reliably to values calculated using high-energy approximations.

II. EXPERIMENTAL METHOD

The apparatus and experimental technique used for our measurements have been described in de-